Inorg. Chem. **2006**, *45*, 137–146

Platinum(II) Complexes with Pyridyl Azolate-Based Chelates: Synthesis, Structural Characterization, and Tuning of Photo- and Electrophosphorescence

Sheng-Yuan Chang,[†] Jakka Kavitha,[†] Shih-Wen Li,[†] Chan-Shou Hsu,[†] Yun Chi,*[,†] Yu-Shan Yeh,[‡] Pi-Tai Chou,*[,‡] Gene-Hsiang Lee,[‡] Arthur J. Carty,*[,§] Yu-Tai Tao,[||] and Chin-Hsiung Chien[||]

Department of Chemistry, National Tsing Hua University, Hsinchu 300, Taiwan, Department of Chemistry and Instrumentation Center, National Taiwan University, Taipei 106, Taiwan, Steacie Institute for Molecular Sciences, National Research Council, Ontario K1A 0R6, Canada, and Institute of Chemistry, Academia Sinica, Taipei 115, Taiwan

Received August 16, 2005

A new series of luminescent platinum(II) azolate complexes with a formula of $[Pt(N\wedge N)_2]$, in which N∧N = mppz (**1**), bppz (**2a**), bzpz (**2b**), bmpz (**2c**), bqpz (**2d**), fppz (**3a**), hppz (**3b**), bptz (**4**), hptz (**5**), were synthesized, and their photophyscial properties were examined. Single-crystal X-ray diffraction studies of **2c** and **3b** revealed a planar molecular geometry, in which the N∧N chelates adopt a trans configuration and show notable interligand C–H···N hydrogen bonding within the complex. Interesting intermolecular interactions were observed in the solid state. Complex **2c** formed a slipped-stack structure with a Pt···Pt separation distance of 6.432 Å, while complex **3b** showed a columnar stacking with the molecules oriented in an alternating order in relation to the chain axis, giving a much reduced Pt···Pt distance of 3.442 Å. The lowest absorption band for all complexes revealed strong state mixings between the singlet and triplet (MLCT and intraligand $\pi\pi^*$) manifolds. Complexes **1** and **2** showed mixed ^{3}MLCT and $^3\pi\pi$ phosphorescence in fluid solution. While radiationless deactivation was apparently dominant for complxes **3**–**5** in solution, resulting in rather weak emission, strong phosphorescence was observed in the room-temperature solid state with the peak wavelength being significantly red shifted compared to that in solution. The emission nature has been tentatively assigned to be ^{3}MMLCT in character. OLED devices with a multilayer configuration of ITO/NPB/CBP:**2a**/BCP/Alq_3/LiF/Al were successfully fabricated using a CBP layer doped with various amount of **2a**, ranging from 6 to 100%, as the emitting layer. A substantial red shift with increasing doping concentrations was observed in electroluminescence. With a neat film of **2a**, the device showed a green emission with λ_{max} at 556 nm and an external QE of ∼1.6% at a driving current of 20 mA. Similarly, for the device using a neat film of **3a**, an electroluminescence centered at 616 nm with a slightly reduced external QE of ∼2.1% was recorded. Aggregation of platinum(II) complexes in the solid state was proposed to account for the large red-shift in electroluminescence.

Introduction

Organometallic complexes with a third-row transition metal element are crucial for the fabrication of highly efficient organic light-emitting diodes (OLEDs).[1] The strong spin−orbit coupling promotes efficient intersystem crossing from the singlet to the triplet excited-state manifold. As a result, numerous attempts have been made to exploit third-row transition metal complexes as phosphorescent dopant emitters,[2−4] among which quite a few osmium(II)[2] and iridium(III)[3] complexes have been reported to exhibit excel-

* To whom correspondence should be addressed. E-mail: ychi@mx.nthu.edu.tw (Y.C.); chop@ntu.edu.tw (P.-T.C.); acarty@pco-bcp.gc.ca (A.J.C.).
[†] Department of Chemistry, National Tsing Hua University.
[‡] Department of Chemistry and Instrumentation Center, National Taiwan University.
[§] Steacie Institute for Molecular Sciences, National Research Council.
[||] Institute of Chemistry, Academia Sinica.

(1) (a) Baldo, M. A.; O'Brien, D. F.; You, Y.; Shoustikov, A.; Sibley, S.; Thompson, M. E.; Forrest, S. R. *Nature* **1998**, *395*, 151. (b) Baldo, M. A.; Thompson, M. E.; Forrest, S. R. *Pure Appl. Chem.* **1999**, *71*, 2095. (c) Gong, X.; Ostrowski, J. C.; Bazan, G. C.; Moses, D.; Heeger, A. J. *Appl. Phys. Lett.* **2002**, *81*, 3711.

10.1021/ic051393b CCC: $33.50
Published on Web 12/09/2005

lent device performances. More recently, a breakthrough has been made with ruthenium(II)-based OLED devices,[4] the results of which may attract attention from an economic viewpoint.

Recently, the efficiency of OLEDs was dramatically increased to, for example, ≥15% for external quantum efficiency by employing either green [$Ir(ppy)_3$][5] or red [$Os(fptz)_2(PPh_2Me)_2$][6] emitters with a multilayer device architecture. Despite the developments with iridium(III) and osmium(II), attempts to further expand the application of other analogues, such as platinum(II) emitting materials, for efficient OLED applications have still encountered many obstacles.[7] For example, the PtOEP (H_2OEP = octaethylporphyrin) commonly exhibits a ligand-based $\pi\pi^*$ phosphorescence with a lifetime up to 30−50 μs. Accordingly, saturation of the emission signals and a rapid drop in device efficiency at high driving currents are expected. A second factor contributing to the inferior efficiency is the planar geometry which could easily induce the formation of aggregates[8] or excimers[9] via efficient $\pi-\pi$ stacking at the vacant coordination sites on the Pt(II) atom. A design aimed at color tuning and suppressing the self-aggregation of Pt(II) complexes is needed to exploit the full potential of Pt(II) emitters; among these methods, the introduction of the acetylide ligand has shown its versatility in color tuning,[10] while employing rigid architecture, such as the camphor-based ligand, is an alternative strategy for alleviating the aggregation.[11] One expects that this camphor-based substituent on the ligands would strictly inhibit the columnar alignment of complex molecules as well as the occurrence of the direct Pt···Pt bonding in the solid state. OLEDs with efficient saturated red emission have been successfully fabricated using this camphor-based Pt(II) dopant.[11]

In this study, we focused on the preparation, characterization, and photophysical properties of a series of readily sublimable and thermally robust Pt(II) pyridyl azolate complexes, **1**−**5**. The azolate ligands employed in this investigation are superior to camphor-based ligand chromophores because of their greater structural tuning capability and flexibility at the ligand sites. Thus, the substituent fine-tuning photophysical properties are expected, especially in the solid state. Among complexes **1**−**5**, several derivatives, such as **1**, **2d**, and **4**, exhibit room-temperature phosphorescence in the fluid and/or solid states, assigned to, depending on ancillary ligands, ^{3}MLCT/$^3\pi\pi^*$, $^3\pi\pi^*$, or ^{3}MMLCT transitions. We expected that the various fundamental properties elaborated in this study would be beneficial to the future development of Pt(II) emitting materials, as complexes **2a** and **3a** are well suited for use as phosphorescent OLEDs.

Experimental Section

General Procedures. All reactions were performed under nitrogen. Solvents were distilled from appropriate drying agents prior to use. Commercially available reagents were used without further purification unless otherwise stated. All reactions were monitored by TLC with Merck precoated glass plates (0.20 mm with fluorescent indicator UV_{254}). Compounds were visualized with UV light irradiation at 254 and 365 nm. Flash column chromatography was carried out using silica gel from Merck (230−400 mesh). Mass spectra were obtained on a JEOL SX-102A instrument operating in electron impact (EI) or fast atom bombardment (FAB) mode. ^{1}H and ^{13}C NMR spectra were recorded on a Bruker-400 or INOVA-500 instrument; chemical shifts are quoted with respect to the internal standard, tetramethylsilane, for ^{1}H and ^{13}C NMR data. Elemental analysis was carried out with a Heraeus CHN−O Rapid Elementary Analyzer. $Pt(DMSO)_2Cl_2$ was prepared according to the literature method.[12] 3-Trifluoromethyl- and 3-heptafluoropropyl-substituted 5-(2-pyridyl) pyrazoles (fppz)H and (hppz)H were prepared via the reaction of 2-acetylpyridine with either ethyl trifluoroacetate or ethyl perfluorobutanoate, followed by treatment with hydrazine hydrate in ethanol solution,[13] while 3-methyl-5-(2-pyridyl) pyrazole (mppzH), 3-*tert*-butyl-5-(2-pyridyl) pyrazole (bppzH), 1-(5-*tert*-butyl-2H-pyrazol-3-yl) isoquinoline (bqpzH), 3-*tert*-butyl-5-(2-pyrazine) pyrazole (bzpzH), and 3-*tert*-butyl-5-(5-methyl-2-pyrazine) pyrazole (bmpzH) were prepared from reactions involving ethyl picolinate, ethyl isoquinaldate, ethyl pyrazinecarboxylate, or ethyl 5-methylpyrazine-2-carboxylate with either acetone or pinacolone, respectively, followed by treatment of the condensation product with hydrazine hydrate under similar conditions. The respective 2-pyridyl triazole ligands, namely, 5-*tert*-butyl-3-(pyridin-2-yl)-1H-1,2,4-triazole (bptzH) and 5-heptafluoropropyl-3-(pyridin-2-yl)-1H-1,2,4-triazole (hptzH), were synthesized using previously reported procedures.[14] Their structures are depicted in Chart 1.

Spectroscopic and Dynamic Measurements. Steady-state absorption and emission spectra were recorded on a Hitachi (U-3310)

(2) (a) Carlson, B.; Phelan, G. D.; Kaminsky, W.; Dalton, L.; Jiang, X.; Liu, S.; Jen, A. K. Y. *J. Am. Chem. Soc.* **2002**, *124*, 14162. (b) Bernhard, S.; Gao, X.; Malliaras, G. G.; Abruna, H. D. *Adv. Mater.* **2002**, *14*, 433. (c) Tung, Y. L.; Wu, P. C.; Liu, C. S.; Chi, Y.; Yu, J. K.; Hu, Y. H.; Chou, P. T.; Peng, S. M.; Lee, G. H.; Tao, Y.; Carty, A. J.; Shu, C. F.; Wu, F. I. *Organometallics* **2004**, *23*, 3745.
(3) (a) Lamansky, S.; Djurovich, P.; Murphy, D.; Abdel-Razzaq, F.; Lee, H. E.; Adachi, C.; Burrows, P. E.; Forrest, S. R.; Thompson, M. E. *J. Am. Chem. Soc.* **2001**, *123*, 4304. (b) Tsuboyama, A.; Iwawaki, H.; Furugori, M.; Mukaide, T.; Kamatani, J.; Igawa, S.; Moriyama, T.; Miura, S.; Takiguchi, T.; Okada, S.; Hoshino, M.; Ueno, K. *J. Am. Chem. Soc.* **2003**, *125*, 12971.
(4) Tung, Y. L.; Lee, S. W.; Chi, Y.; Chen, L. S.; Shu, C. F.; Wu, F. I.; Carty, A. J.; Chou, P. T.; Peng, S. M.; Lee, G. H. *Adv. Mater.* **2005**, *17*, 1059.
(5) Adachi, C.; Baldo, M. A.; Forrest, S. R.; Lamansky, S.; Thompson, M. E.; Kwong, R. C. *Appl. Phys. Lett.* **2001**, *78*, 1622.
(6) Tung, Y. L.; Lee, S. W.; Chi, Y.; Tao, Y. T.; Chien, C. H.; Cheng, Y. M.; Chou, P. T.; Peng, S. M.; Liu, C. S. *J. Mater. Chem.* **2005**, *15*, 460.
(7) (a) Kwong, R. C.; Sibley, S.; Dubovoy, T.; Baldo, M.; Forrest, S. R.; Thompson, M. E. *Chem. Mater.* **1999**, *11*, 3709. (b) Che, C. M.; Hou, Y. J.; Chan, M. C. W.; Guo, J.; Liu, Y.; Wang, Y. *J. Mater. Chem.* **2003**, *13*, 1362.
(8) (a) Dungey, K. E.; Thompson, B. D.; Kane-Maguire, N. A. P.; Wright, L. L. *Inorg. Chem.* **2000**, *39*, 5192. (b) Chan, S. C.; Chan, M. C. W.; Wang, Y.; Che, C. M.; Cheung, K. K.; Zhu, N. *Chem.—Eur. J.* **2001**, *7*, 4180. (c) Lin, Y. Y.; Chan, S. C.; Chan, M. C. W.; Hou, Y. J.; Zhu, N.; Che, C. M.; Liu, Y.; Wang, Y. *Chem.—Eur. J.* **2003**, *9*, 1263. (d) Ma, B.; Li, J.; Djurovich, P. I.; Yousufuddin, M.; Bau, R.; Thompson, M. E. *J. Am. Chem. Soc.* **2005**, *127*, 28.
(9) (a) Pettijohn, C. N.; Jochnowitz, E. B.; Chuong, B.; Nagle, J. K.; Vogler, A. *Coord. Chem. Rev.* **1998**, *171*, 85. (b) Connick, W. B.; Geiger, D.; Eisenberg, R. *Inorg. Chem.* **1999**, *38*, 3264. (c) Hissler, M.; McGarrah, J. E.; Connick, W. B.; Geiger, D. K.; Cummings, S. D.; Eisenberg, R. *Coord. Chem. Rev.* **2000**, *208*, 115.
(10) Lu, W.; Mi, B. X.; Chan, M. C. W.; Hui, Z.; Che, C. M.; Zhu, N.; Lee, S. T. *J. Am. Chem. Soc.* **2004**, *126*, 4958.
(11) Kavitha, J.; Chang, S. Y.; Chi, Y.; Yu, J. K.; Hu, Y. H.; Chou, P. T.; Peng, S. M.; Lee, G. H.; Tao, Y. T.; Chien, C. H.; Carty, A. J. *Adv. Funct. Mater.* **2005**, *15*, 223.
(12) Cini, R.; Donati, A.; Giannettoni, R. *Inorg. Chim. Acta*. **2001**, *315*, 73.

Chart 1

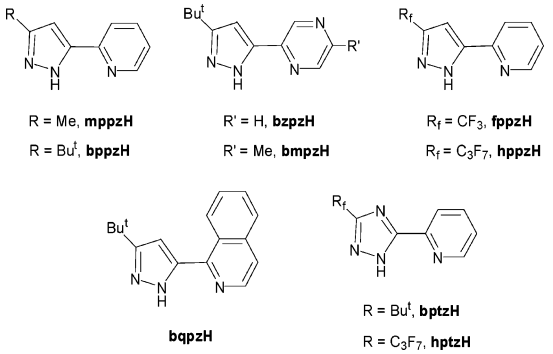

spectrophotometer and an Edinburgh (FS920) fluorimeter, respectively. Both the wavelength-dependent excitation and the emission response of the fluorimeter were calibrated. A configuration of front-face excitation was used to measure the emission of the solid sample, in which the cell was made by assembling two edge-polished quartz plates with various Teflon spacers. Lifetime studies were performed with an Edinburgh FL 900 photon-counting system with a hydrogen-filled or nitrogen lamp as the excitation source. Data were analyzed using a nonlinear least squares procedure in combination with an iterative convolution method. The emission decays were analyzed by the sum of the exponential functions, which allowed partial removal of the instrument time broadening and consequently renderes a temporal resolution of ~200 ps.

To determine the photoluminescence quantum yield in solution, samples were degassed by three freeze−pump−thaw cycles under vigorous stirring conditions. 4-(Dicyanomethylene)-2-methyl-6-(*p*-dimethylaminostyryl)-4H-pyran (DCM, λ_{em} = 615 nm, Exciton, Inc.) in methanol was used as a reference, assuming a quantum yield of 0.43 with a 430 nm excitation.[15] An integrating sphere (Labsphere) was applied to measure the quantum yield in the solid state, for which the solid sample film was prepared via either spin-coating or vapor-deposition methods and was excited by a 371 or 480 nm Ar^+ laser line; an intensified charge-coupled detector was used for subsequent quantum yield analyses of the resulting luminescence. To obtain the PL quantum yield in solid state, the emission was collected via an integrating sphere, and the quantum yield was calculated according to a reported method.[16] The values were taken to be the average of three separated measurements.

Synthesis of Pt(mppz)$_2$ (1). 3-Methyl-5-(2-pyridyl) pyrazole (mppzH, 83 mg, 0.52 mmol) was added slowly at room temperature to a suspension of NaH (15 mg, 0.63 mmol) in 15 mL of THF. After being stirred for 1.5 h, the solution was filtered and transferred into a reaction flask loaded with 100 mg of $Pt(DMSO)_2Cl_2$ (0.24 mmol) and 10 mL of THF. The solution was brought to reflux for 12 h. After that, the solvent was evaporated under vacuum, and 60 mL of CH_2Cl_2 was added to extract the product. The extract was then washed with water, dried over anhydrous Na_2SO_4, and concentrated to dryness, giving a yellowish green powder. Further purification was conducted using vacuum sublimation (160 °C, 220 mTorr), yielding 80 mg of Pt(mppz)$_2$ as bright green needles (0.16 mmol, 65%). Other Pt(II) complexes, **2**−**4**, were synthesized using $Pt(DMSO)_2Cl_2$ and the corresponding neutral ligands under similar reaction conditions.

(13) (a) Thiel, W. R.; Eppinger, J. *Chem.—Eur. J.* **1997**, *3*, 696. (b) Singh, S. P.; Kumar, D.; Jones, B. G.; Threadgill, M. D. *J. Fluorine Chem.* **1999**, *94*, 199.
(14) (a) Kubota, S.; Uda, M.; Nakagawa, T. *J. Heterocycl. Chem.* **1975**, *12*, 855. (b) Funabiki, K.; Noma, N.; Kuzuya, G.; Matsui, M.; Shibata, K. *J. Chem. Res. (M)* **1999**, 1301.
(15) Drake, J. M.; Lesiecki, M. L.; Camaioni, D. M. *Chem. Phys. Lett.* **1985**, *113*, 530.

Data for 1. MS (EI, 70 eV), observed (actual) [assignment]: *m*/*z* 511 (511) [M^+]. ^{1}H NMR (500 MHz, $CDCl_3$, 294 K): δ 10.64 (d, $^3J_{HH}$ = 6.0 Hz, 2H), 7.86 (t, $^3J_{HH}$ = 8.0 Hz, $^3J_{HH}$ = 8.0 Hz, 2H), 7.55 (d, $^3J_{HH}$ = 8.0 Hz, 2H), 7.28 (t, $^3J_{HH}$ = 6.0 Hz, $^3J_{HH}$ = 6.0 Hz, 2H), 6.43 (s, 2H), 2.45 (s, 6H). ^{13}C NMR (125 MHz, $CDCl_3$, 294K): δ 154.7 (C_{py}), 152.5 (C_{pz}), 150.3 (CH_{py}), 147.6 (C_{pz}), 139.1 (CH_{py}), 121.6 (CH_{py}), 118.2 (CH_{py}), 103.0 (CH_{pz}), 14.0 (CH_3). Anal. Calcd for $C_{18}H_{16}N_6Pt$: C, 42.27; N, 16.43; H, 3.15. Found: C, 42.08; N, 16.38; H, 3.49.

Data for 2a. MS (EI, 70 eV), observed (actual) [assignment]: *m*/*z* 595 (595) [M^+]. ^{1}H NMR (400 MHz, $CDCl_3$, 294 K): δ 10.79 (d, $^3J_{HH}$ = 6.0 Hz, 2H), 7.82 (ddd, $^3J_{HH}$ = 7.9 Hz, $^3J_{HH}$ = 7.6 Hz, $^4J_{HH}$ = 1.2 Hz, 2H), 7.55 (d, $^3J_{HH}$ = 7.9 Hz, 2H), 7.19 (ddd, $^3J_{HH}$ = 7.6 Hz, $^3J_{HH}$ = 6.0 Hz, $^4J_{HH}$ = 1.2 Hz, 2H), 6.49 (s, 2H), 1.42 (s, 18H). ^{13}C NMR (125 MHz, $CDCl_3$, 294K): δ 161.4 (C_{py}), 155.4 (C_{pz}), 152.3 (CH_{py}), 149.4 (C_{pz}), 138.8 (CH_{py}), 120.7 (CH_{py}), 117.8 (CH_{py}), 99.4 (CH_{pz}), 32.6 ($C_{t-butyl}$), 31.0 (CH_3). Anal. Calcd for $C_{24}H_{28}N_6Pt$: C, 48.40; N, 14.11; H, 4.74. Found: C, 48.31; N, 14.10; H, 4.88.

Data for 2b. MS (EI, 70 eV), observed (actual) [assignment]: *m*/*z* 597 (597) [M^+], 582 (582) [$M^+ - CH_3$]. ^{1}H NMR (500 MHz, $CDCl_3$, 294 K): δ 10.54 (d, $^3J_{HH}$ = 3.8 Hz, 2H), 8.83 (s, 2H), 8.38 (d, $^3J_{HH}$ = 3.8 Hz, 2H), 6.50 (s, 2H), 1.43 (s, 18H). ^{13}C NMR (125 MHz, $CDCl_3$, 294 K): δ 162.4 (C_{py}), 149.7 (C_{pz}), 145.9 (C_{pz}), 144.2 (CH_{py}), 141.9 (CH_{py}), 140.6 (CH_{py}), 100.9 (CH_{pz}), 32.7 ($C_{t-butyl}$), 30.9 (CH_3). Anal. Calcd for $C_{22}H_{26}N_8Pt$: C, 44.22; N, 18.75; H, 4.39. Found: C, 43.94; N, 19.21; H, 4.60.

Data for 2c. MS (EI, 70 eV), observed (actual) [assignment]: *m*/*z* 626 (625) [M^+], 611 (610) [$M^+ - CH_3$]. ^{1}H NMR (500 MHz, $CDCl_3$, 294 K): δ 10.65 (s, 2H), 8.80 (s, 2H), 6.55 (s, 2H), 2.71 (s, 6H) 1.43 (s, 18H). ^{13}C NMR (125 MHz, $CDCl_3$, 294 K): δ 162.1 (C_{py}), 151.9 (C_{pz}), 146.9 (C_{pz}), 146.5 (CH_{py}), 143.9 (CH_{py}), 139.5 (CH_{py}), 99.9 (CH_{pz}), 32.7 ($C_{t-butyl}$), 30.9 (CH_3), 21.6 (CH_3). Anal. Calcd for $C_{24}H_{30}N_8Pt$: C, 46.07; N, 17.91; H, 4.83. Found: C, 46.15; N, 17.70; H, 5.02.

Data for 2d. MS (FAB), observed (actual) [assignment]: *m*/*z* 696 (696) [M^+]. ^{1}H NMR (400 MHz, CD_2Cl_2, 294 K): δ 10.98 (d, *J* = 5.6 Hz, 2H), 8.82 (d, *J* = 7.9 Hz, 2H), 7.95 (d, *J* = 7.9 Hz, 2H), 7.86 (t, *J* = 7.0 Hz, 2H), 7.77 (t, *J* = 7.4 Hz, 2H),7.66 (d, *J* = 5.7 Hz, 2H), 7.06 (s, 2H), 1.55(s, 18H). Anal. Calcd for $C_{32}H_{32}N_6Pt$: C, 55.24; H, 4.64; N, 12.08. Found: C, 54.88; H, 4.94; N, 11.98.

Data for 3a. MS (EI, 70 eV), observed (actual) [assignment]: *m*/*z* 619 (619) [M^+], 407 (407) [M^+ − fppz]. ^{1}H NMR (400 MHz, acetone-d_6, 294 K): δ 10.29 (d, $^3J_{HH}$ = 6.0 Hz, 2H), 8.19 (ddd, $^3J_{HH}$ = 7.6 Hz, $^3J_{HH}$ = 7.6 Hz, $^4J_{HH}$ = 1.4 Hz, 2H), 7.94 (d, $^3J_{HH}$ = 7.6 Hz, 2H), 7.47 (ddd, $^3J_{HH}$ = 7.6 Hz, $^3J_{HH}$ = 6.0 Hz, $^4J_{HH}$ = 1.4 Hz, 2H), 7.07 (s, 2H). ^{19}F (470 MHz, toluene-d_8, 294 K): δ −60.70 (s, CF_3). Anal. Calcd for $C_{18}H_{10}F_6N_6Pt$: C, 34.90; N, 13.57; H, 1.63. Found: C, 34.44; N, 13.12; H, 1.78.

Data for 3b. MS (EI, 70 eV), observed (actual) [assignment]: *m*/*z* 820 (819) [M^+]. ^{1}H NMR (500 MHz, THF-d_8, 294 K): δ 10.53 (d, $^3J_{HH}$ = 6.0 Hz, 2H), 8.14 (ddd, $^3J_{HH}$ = 7.5 Hz, $^3J_{HH}$ = 7.5 Hz, $^4J_{HH}$ = 1.0 Hz, 2H), 7.95 (d, $^3J_{HH}$ = 7.5 Hz, 2H), 7.48 (ddd, $^3J_{HH}$ = 7.5 Hz, $^3J_{HH}$ = 6.0 Hz, $^4J_{HH}$ = 1.0 Hz, 2H), 7.13 (s, 2H). ^{19}F (470 MHz, THF-d_8, 294 K): δ −80.83 (t, $^3J_{FF}$ = 8.5 Hz, CF_3), −109.06 (dd, $^3J_{FF}$ = 19.3 Hz, $^3J_{FF}$ = 8.5 Hz, CF_2), −127.31 (s, CF_2). Anal. Calcd for $C_{22}H_{10}F_{14}N_6Pt$: C, 32.25; N, 10.26; H, 1.23. Found: C, 32.23; N, 10.01; H, 1.51.

Data for 4. MS (EI, 70 eV), observed (actual) [assignment]: *m*/*z* 597 (597) [M^+]. ^{1}H NMR (400 MHz, $CDCl_3$, 294 K): δ 10.49 (d, $^3J_{HH}$ = 6.0 Hz, 2H), 8.07 (d, $^3J_{HH}$ = 7.6 Hz, 2H), 8.00 (ddd, $^3J_{HH}$ = 7.6 Hz, $^3J_{HH}$ = 7.6 Hz, $^4J_{HH}$ = 1.2 Hz, 2H), 7.40 (ddd,

Table 1. Crystal Data and Refinement Parameters for Complexes **2c** and **3b**

	2c	**3b**
formula	$C_{24}H_{30}N_8Pt$	$C_{22}H_{10}F_{14}N_6Pt$
mol wt	625.65	819.45
cryst syst	monoclinic	monoclinic
space group	$P2_1/c$	$C2/c$
cryst size (mm^3)	$0.25 \times 0.10 \times 0.06$	$0.23 \times 0.05 \times 0.03$
morphology	red slab	orange needle
a (Å)	6.4321(2)	18.1823(3)
b (Å)	13.3584(5)	20.0340(4)
c (Å)	30.8313(11)	6.8846(1)
β (deg)	91.8682(11)	92.5381(11)
V ($Å^3$)	2647.7(2)	2505.35(7)
Z	4	4
ρ_{calcd} (g/cm^3)	1.570	2.173
temp (K)	295(2)	295(2)
μ (mm^{-1})	5.326	5.731
reflns collected	25258	15234
independent reflns	6082 [R(int) = 0.0706]	2887 [R(int) = 0.0546]
R_F, $R_w(F^2)$ (all data)[a]	0.0835, 0.1313	0.0961, 0.1799
R_F, $R_w(F^2)$ [$I > 2\sigma(I)$][a]	0.0531, 0.1130	0.0563, 0.1507
GOF	1.095	1.124

[a] $R_F = \sum||F_o| - |F_c||/\sum|F_o|$; $R_w(F^2) = [\sum w|F_o^2 - F_c^2|^2/\sum w(F_o^4)]^{1/2}$.

Table 2. Selected Bond Length (Å) and Angles (deg) for Complexes **2c** and **3b**

2c			
Pt(1)−N(1)	2.016(5)	Pt(1)−N(2)	1.994(6)
Pt(1)−N(5)	2.028(5)	Pt(1)−N(6)	1.986(6)
Pt(1)···Pt(1)	6.432		
H(1A)···N(7)	2.256	H(13A)···N(3)	2.296
N(1)−Pt(1)−N(2)	78.8(2)	N(5)−Pt(1)−N(6)	79.2(2)
N(1)−Pt(1)−N(6)	101.0(2)	N(2)−Pt(1)−N(5)	101.0(2)
3b			
Pt−N(1)	2.056(8)	Pt−N(2)	1.979(7)
Pt···Pt	3.442	H(1A)···N(3)	2.319
N(1)−Pt(1)−N(2)	79.6(3)	N(1)−Pt(1)−N(2′)	100.4(3)

$^3J_{HH}$ = 7.6 Hz, $^3J_{HH}$ = 6.0 Hz, $^4J_{HH}$ = 1.2 Hz, 2H), 1.49 (s, 18H). Anal. Calcd for $C_{22}H_{26}N_8Pt$: C, 44.22; N, 18.75; H, 4.39. Found: C, 44.12; N, 18.69; H, 4.48.

Synthesis of Pt(hptz)$_2$ (5). A solution of K_2PtCl_4 (100 mg, 0.24 mmol) and hptzH (167 mg, 0.53 mmol) in a mixture of ethanol (15 mL) and water (5 mL) was heated at 80 °C for about 16 h. After the mixture was cooled to room temperature, the precipitate was collected, washed with diethyl ether, and dried under vacuum to give Pt(hptz)$_2$ as an orange solid (78 mg, 0.096 mmol) in a 40% yield.

Data for 5. MS (EI, 70 eV), observed (actual) [assignment]: m/z 822 (821) [M^+]. ^{1}H NMR (500 MHz, THF-d_8, 294 K): δ 10.31 (d, $^3J_{HH}$ = 6.0 Hz, 2H), 8.31 (t, $^3J_{HH}$ = 7.0 Hz, 2H), 8.20 (d, $^3J_{HH}$ = 7.0 Hz, 2H), 7.74 (t, $^3J_{HH}$ = 6.0 Hz, 2H). Anal. Calcd for $C_{22}H_8F_{14}N_8Pt$: C, 29.24; N, 13.64; H, 0.98. Found: C, 28.74; N, 13.37; H, 1.14.

X-ray Diffraction Studies. Single-crystal X-ray diffraction data were measured on a Bruker SMART Apex CCD diffractometer using μ(Mo Kα) radiation (λ = 0.71073 Å). The data collection was executed using the SMART program; cell refinement and data reduction were performed with the SAINT program. The structure was determined using the SHELXTL/PC program and refined using full-matrix least squares. Crystallographic refinement parameters of complexes **2c** and **3b** and their selective bond distances and angles are summarized in Tables 1 and 2, respectively.

OLED Fabrication. Charge-transporting materials such as NPB {4,4′-bis[*N*-(1-naphthyl)-*N*-phenylamino]biphenyl} and Alq_3 [tris-(8-hydroxyquinolinato) aluminum(III)], as well as the host material CBP (4,4′-*N*,*N*′-dicarbazolyl-1,1′-biphenyl), were synthesized according to literature procedures,[17] and were sublimed twice through a temperature-gradient sublimation system before use. BCP (2,9-dimethyl-4,7-diphenyl-1,10-phenanthroline) was obtained from Aldrich. Patterned ITO-coated glass substrates (sheet resistance ≤ 30 Ω/□) with an effective individual device area of 3.14 mm^2 were cleaned by sonication in a detergent solution, water, and ethanol and then dried by a flow of nitrogen. The substrates were further treated with oxygen plasma for 3 min before being loaded into the vacuum chamber. Various organic layers were deposited sequentially at a rate of 0.1−0.3 nm/s under a pressure of 2×10^{-5} Torr in an Ulvac Cryogenic deposition system. Phosphorescent dopants were coevaporated with CBP via two independent sources. A thin layer of LiF (1 nm) and a thick layer of Al (150 nm) followed as the cathode. The current−voltage−luminance of the devices was measured in ambient conditions with a Keithley 2400 Source meter and a Newport 1835C Optical meter equipped with an 818ST silicon photodiode. The EL spectrum was obtained using a HITACHI F4500 spectrofluorimeter. The active area of the device was 3.14 mm^2 and that of the silicon photodiode was 100 mm^2. The device was placed close to the photodiode so that all the forward light went to the photodiode. The luminance was calibrated using a PR-650 Spectrascan Colorimeter (Photo Research, USA). The external quantum efficiency was calculated according to the method previously described.[18] The luminous flux (lm) is defined[19] by $P_v = K_m \int_\lambda P_{e,\lambda} V(\lambda) d\lambda$, where K_m is the maximum luminous efficiency (683 lm/W), $P_{e,\lambda}$ is the spectral concentration of radiant flux, and $V(\lambda)$ is the relative photonic luminous efficiency function; the luminance (cd/m^2) is defined by luminous flux/πa, where a is the device area. The luminous efficiency (cd/A) is defined by luminous flux/πI, where I is the current, and the power efficiency is defined as luminous flux/IV, where V is the applied voltage.

Results and Discussion

Synthesis and Characterization. The chelating pyrazole ligands are derived from a two-step synthetic reaction involving Claisen condensation, followed by treatment with hydrazine in a refluxing ethanol solution. Triazole ligands are prepared from 2-pyridyl carboximidamide or carboxamidrazone using methods reported in the literature.[14] These ligands are represented as (N∧N)H, implying that the N∧N chelating anions can be easily produced by deprotonation of the neutral ligands with a suitable base.

The targeted Pt(II) emitting materials (Chart 2) were then obtained via two distinctive pathways. The first one incorporates an in situ generation of the sodium salt of the $(N\wedge N)^-$ anion, followed by treatment with a suspension of [$PtCl_2$-$(DMSO)_2$] in refluxing THF; while the second involves direct reaction of the neutral (N∧N)H ligands with K_2PtCl_4 in ethanol to yield Pt(II) complexes with the formula [Pt-$(N\wedge N)_2$]. Both methods gave satisfactory yields, and detailed procedures are given in the Experimental Section. In addition, all Pt(II) complexes showed good stability in both the fluid and solid states, but their solubility in organic solvents varied

(16) de Mello, J. C.; Wittmann, H. F.; Friend, R. H. *Adv. Mater.* **1997**, *9*, 230.
(17) (a) Sonsale, A. Y.; Gopinathan, S.; Gopinathan, C. *Indian J. Chem.* **1976**, *14*, 408. (b) Koene, B. E.; Loy, D. E.; Thompson, M. E. *Chem. Mater.* **1998**, *10*, 2235.

Chart 2

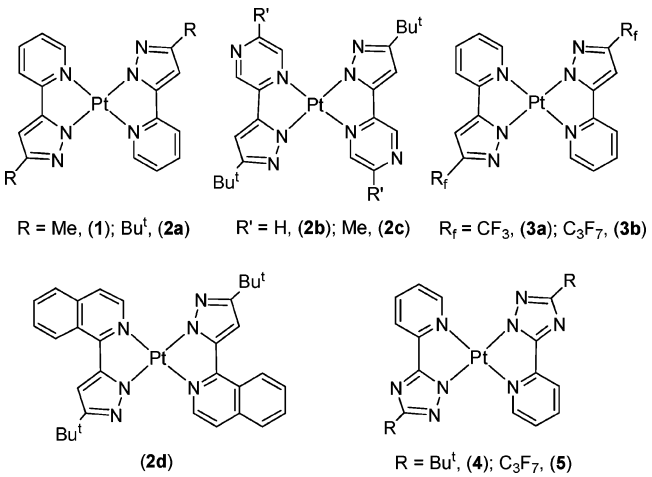

according to the nature of the ligands and the associated alkyl substituents. For example, pyridyl pyrazolate complexes **1** and **2a** showed sparse solubility in organic solvents such as $CHCl_3$, CH_2Cl_2, and THF at room temperature, while the pyrazine- and isoquinoline-substituted complexes **2b**, **2c**, and **2d** were significantly more soluble under identical conditions. For the fluorinated complexes, **3a**, **3b**, and **5**, although the solubility in solvents improved with the increasing chain length of the fluoroalkyl substituent (i.e., CF_3 vs C_3F_7), they tend to exhibit relatively poor solubility at elevated temperatures and rapidly form microcrystalline solids when the solution is cooled to room temperature. On the basis of these experimental facts, the Pt(II) complexes **2b**, **2c**, and **2d** were best purified by routine recrystallization, while vacuum sublimation was employed for separation and purification of other Pt(II) products.

Complex **2c** was examined by single-crystal X-ray diffraction analysis to establish its molecular structure. Figure 1 shows the ORTEP diagram of **2c,** along with a stacking diagram showing the $\pi-\pi$ stacking interactions between molecules. The Pt−N(pyrazolate) bond lengths observed in **2c** vary between 1.986(6) and 1.994(6) Å, which are shorter than those of the Pt−N(pyrazine) (2.016(5) and 2.028(5) Å). This difference reflects the stronger bonding to the anionic pyrazolate fragments versus that of the neutral pyrazine; the latter are within the range reported for those of diimine complexes [Pt(diimine)Cl_2] (1.992−2.015Å) and others.[20] Moreover, interesting intermolecular interactions were observed in the crystal lattice, for which the molecules showed a slipped packing arrangement with one bmpz ligand residing over the center of adjacent molecule. Rather short interplanar $\pi-\pi$ stacking distances of ~3.36 Å were observed between each molecule, indicating the presence of a strong $\pi-\pi$ noncovalent interaction. However, the Pt···Pt separation was calculated to be 6.432 Å along the column, which is too long for any significant Pt−Pt contacts, such as those observed in several dimeric structures of cyclometalated Pt(II) complexes (3.15−3.76 Å)[21] to be expected.

In addition, unusually short N···H contacts (2.256 and 2.296 Å) were detected between the ortho H atom of the

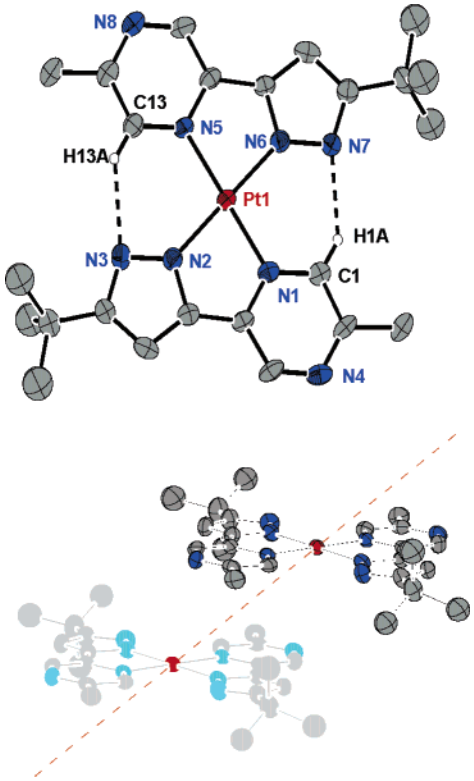

Figure 1. (top) ORTEP diagram of **2c** with thermal ellipsoids shown at the 50% probability level. (bottom) Diagram showing the molecular stacking and closest Pt···Pt contact.

coordinated pyrazine and the uncoordinated N atom of the pyrazolate fragments, H(1A)···N(7) = 2.256 Å and H(13A)···N(3) = 2.296 Å. The tendency of the pyrazolate nitrogen to prefer to connect with the adjacent hydrogen atom is attributable to the greater basicity of the uncoordinated nitrogen atom after the Pt(II) metal coordination. For comparison, it has been reported that the solvated water molecule is held tightly between the pyrazolate ligands of $[Ru(bpy)_2(pz)_2]\cdot H_2O$, and no anhydrous solid material could be isolated.[22] Note that exceedingly strong N−H···N bonding was also observed between the adjacent pyrazolate ligands for the emissive iridium(III) complexes $[(tpy)_2Ir(pzH)_2](CF_3SO_3)$ and $[(tpy)_2Ir(pz_2H)]$.[23]

To offer a direct comparison with respect to **2c**, we also conducted an X-ray structural analysis of the C_3F_7-substituted complex **3b** because it showed very poor solubility and an enhanced tendency to form a needlelike solid during recrystallization. As illustrated in Figure 2, the Pt(II) cation is in the square planar arrangement, and the corresponding Pt−N

(18) Forrest, S. R.; Bradley, D. D. C.; Thompson, M. E. *Adv. Mater*. **2003**, *15*, 1043.

(19) Wyszecki, G.; Stiles, W. S. *Color Science: Concepts and Methods, Quantitative Data and Formulae*; John Wiley & Sons: New York, 1982; p. 259.

(20) (a) Miskowski, V. M.; Houlding, V. H.; Che, C. M.; Wang, Y. *Inorg. Chem.* **1993**, *32*, 2518. (b) Wadas, T. J.; Lachicotte, R. J.; Eisenberg, R. *Inorg. Chem.* **2003**, *42*, 3772.

(21) (a) Chassot, L.; Müller, E.; Von Zelewsky, A. *Inorg. Chem.* **1984**, *23*, 4249. (b) Bailey, J. A.; Miskowski, V. M.; Gray, H. B. *Inorg. Chem.* **1993**, *32*, 369. (c) Ghedini, M.; Pucci, D.; Crispini, A.; Barberio, G. *Organometallics* **1999**, *18*, 2116.

(22) Sullivan, B. P.; Salmon, D. J.; Meyer, T. J.; Peedin, J. *Inorg. Chem.* **1979**, *18*, 3369.

(23) Li, J.; Djurovich, P. I.; Alleyne, B. D.; Tsyba, I.; Ho, N. N.; Bau, R.; Thompson, M. E. *Polyhedron* **2004**, *23*, 419.

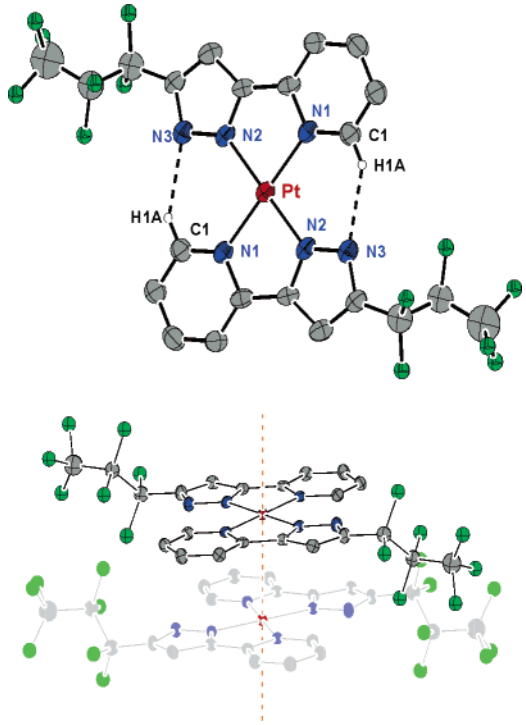

Figure 2. (top) ORTEP diagram of **3b** with thermal ellipsoids shown at the 50% probability level. (bottom) Stacking diagram with an emphasis on the linear Pt···Pt interaction.

distances are not so different from those observed for the previously discussed complex **2c**. However, distinctive intermolecular interactions are observed in its packing diagram, for which the complex molecules are stacked into a column with an alternating staggered orientation along the chain axis. The overall structure is constructed so that each pyridyl fragment is sandwiched by two pyrazolate moieties, and likewise, each pyrazolate fragment is sandwiched by two pyridyl moieties of the neighboring molecules. The resulting noncovalent contact leads to the observed columnar arrangement with a shortened Pt···Pt separation of 3.442 Å, which is almost identical to the average interplanar C−C distances of ~3.35 Å. The related linear Pt···Pt···Pt arrangement has been observed in several of the Pt(II) linear-chain complexes, such as $[Pt(diimine)_2(CN)_2]$, diimine = bipyridine and biisoquinoline.[24]

After the X-ray structural analyses were completed, these Pt(II) complexes were characterized by ^{1}H NMR to obtain their supplementary spectroscopic properties in solution. Of particular interest is the observation of downfield ^{1}H NMR signals in the δ 10.98−10.29 region among complexes **1**−**5**, which are assigned to the interligand C−H···N linkage between two trans-oriented chelating ligands. The proposed H-bonding interaction is reminiscent of those reported for the related pyridyl pyrazolate Os complexes[2c] as well as the cobaloxime complexes.[25] It is believed that this unusual H-bonding, to a certain extent, provides a favorable driving force stabilizing the trans geometry and hence a rigid molecular framework. Certainly, because of the nonlinear C−H···N alignment (vide supra), we cannot rule out the possibility that the C−H···N bonding is caused by the spatial constraint imposed by the ligand arrangement. In contrast to our discovery, the X-ray structural analyses of related Pt(II) complexes such as $Pt(thppy)_2$, thppy = 2-(2′-thienyl) pyridine, revealed that ligated thiophene and pyridine fragments are oriented exclusively in a cis configuration, despite the large distortion and deformation between the ligands.[26] This could be the result of the exceedingly strong trans effect exerted by the carbon donor atom of the ligated thiophene. The net result prevents the ligands from residing at the mutual trans disposition. In contrast, our ligands use weak electron-donating azolate N atoms to form dative bonds with respect to the Pt(II) metal ion. The reduction of the trans effect thus favors the azolate fragments to locate at the mutual trans dispositions.

Table 3. Photophysical Properties of Platinum(II) Complexes **1**−**5**

	λ_{abs}^{max} (ϵ, $M^{-1}cm^{-1}$)	PL λ_{max} (nm)[a]	F	τ (μs)
1	266 (20000), 320 (14300), 338 (10700), 418 (2500), 436 (2400)	495, 516[b] [490[b], 512, 550[b]]	0.21 [2.4×10^{-2}]	0.4 [1.2]
2a	268 (18500), 320 (13100), 340 (10100), 416 (2200), 442 (2100)	494, 518[b] [489, 518, 550[b]]	0.19 [1.1×10^{-2}]	0.4 [0.4]
2b	271 (23200), 313 (11500), 340 (12100), 375 (12700), 473 (2200), 502 (2000)	576, 596[b] [626]	0.82 [6×10^{-4}]	2.4 [0.03]
2c	272 (25000), 314 (11100), 338 (11400), 374 (12100), 480 (2100), 500 (1700)	561, 592[b] [554[b], 581, 623[b], 658[b]]	0.86 [$\leq 10^{-4}$]	2.1 [0.09]
2d	283 (30900), 206 (26800), 351 (30400), 371 (20600), 463 (5200), 484 (4600)	584, 632, 685[b] [593, 634, 680[b]]	0.74 [4×10^{-4}]	13 [0.04]
3a	256 (24000), 310 (19700), 330 (12300), 377 (2900), 389 (2500)	−[c] [595]	– [0.24]	– [0.3]
3b	256 (23400), 310 (19400), 328 (12300), 376 (2900), 388 (2500)	−[c] [552]	– [0.2]	– [0.3]
4	280 (20300), 306 (16500), 326 (11000), 400 (3400), 420 (3155)	482, 512, 540[b] [564]	0.02 [0.16]	0.4 [0.4]
5	258 (21500), 296 (13300), 318 (12300), 360 (3500), 376 (3200)	−[c] [544]	– [0.33]	– [0.3]

[a] The absorption and emission spectra were recorded in degassed THF at room temperature, while the solid-state spectra measured using thin film samples are listed in square brackets. Note that for **3b**, no apparent difference in spectral profile between the thin film and single crystal measurements was observed. [b] Shoulder. [c] Too weak to be observed.

Photophysical Properties. Table 3 summarizes the peak wavelengths of the lowest-energy absorption and other important photophysical data. The room-temperature UV−vis and emission spectra of complexes **2a**−**d** in THF solution are shown in Figure 3. These data allowed us to visualize the spectral variation associated with the derivatization of neutral pyridyl units without altering the anionic pyrazolate segment.

As revealed in Figure 3, it is obvious that the strong absorptions in the UV region (≤350 nm) are derived from a typical ligand-centered $\pi\pi^*$ transition because the corre-

(24) (a) Kato, M.; Sasano, K.; Kosuge, C.; Yamazaki, M.; Yano, S.; Kimura, M. *Inorg. Chem.* **1996**, *35*, 116. (b) Kato, M.; Kosuge, C.; Morii, K.; Ahn, J. S.; Kitagawa, H.; Mitani, T.; Matsushita, M.; Kato, T.; Yano, S.; Kimura, M. *Inorg. Chem.* **1999**, *38*, 1638.

(25) Gupta, B. D.; Singh, V.; Yamuna, R.; Barclay, T.; Cordes, W. *Organometallics* **2003**, *22*, 2670.

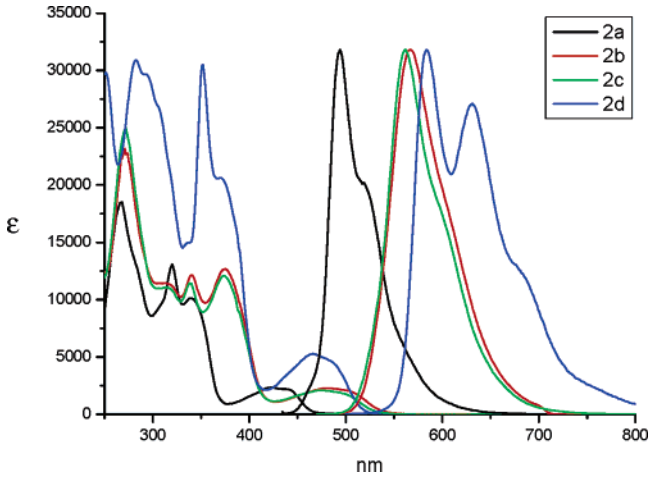

Figure 3. UV−vis absorption and emission spectra of complexes **2a**−**d** in THF at room temperature. Note that the normalized emission spectra were acquired in the degassed condition.

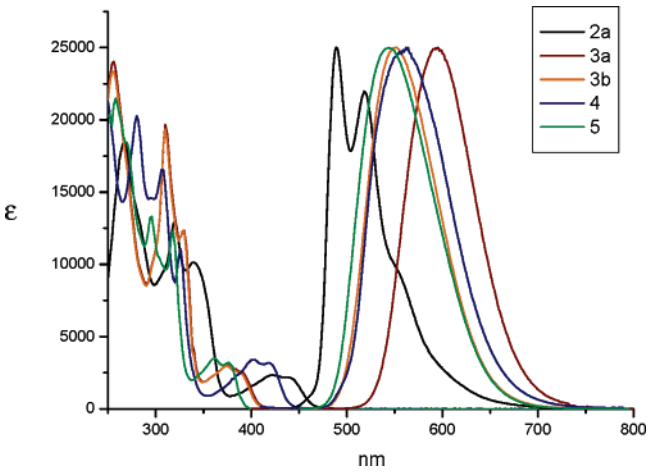

Figure 4. UV−vis absorption spectra of complexes **2a**, **3a**, **3b**, **4**, and **5** recorded in THF at room temperature, and the respective solid-state emission spectra obtained from a thin film sample at room temperature.

sponding transitions were also documented for the free ligands. The lower-lying absorption bands have relatively small extinction coefficients (**2a**, 2200 M^{-1} cm^{-1} at 416 nm; **2b**, 2200 M^{-1} cm^{-1} at 473 nm; **2c**, 2100 M^{-1} cm^{-1} at 480 nm) and are tentatively assigned to the transition incorporating a state mixing among singlet and triplet metal−ligand charge transfer (^{1}MLCT and ^{3}MLCT) and, to a certain extent, the intraligand $^3\pi\pi$ transitions. Interpretation of these MLCT bands may be further complicated by the fact that these bands are clearly composed of two distinctive transitions; similar observations have been documented for the Pt(II) acetylide complexes.[27] Moreover, the close energetics and absorptivity between the ^{1}MLCT and ^{3}MLCT bands suggest that the ^{3}MLCT transition, induced by spin−orbit coupling and the proximal energy levels with respect to ^{1}MLCT, is greatly enhanced and becomes partially allowed. This salient spectral feature is in accordance with data for other recently published Pt(II) metal complexes with two N∧O bidentate chelates or bis(phenoxy)diimine auxiliaries capable of tetradentate bonding.[28] The strong singlet−triplet mixing is unambiguously confirmed by the significant overlap between the UV−vis absorption bands and the leading edge of the respective emission peak profile.

Also shown in Figure 3, complex **2a** exhibits a fairly intensive emission maximized at 494 nm ($\Phi = 0.19$; $\tau = 0.4$ μs) in degassed THF. The fast oxygen quenching rate of 1.78×10^9 M^{-1} s^{-1}, in combination with its spectral mirror image with respect to the lowest-absorption profile, leads us to conclude that the emission mainly originates from a triplet manifold. Similarly, complexes **2b** and **c** also exhibit strong phosphorescence with peak wavelengths at 576 nm ($\Phi = 0.82$; $\tau = 2.4$ μs) and at 561 nm ($\Phi = 0.86$; $\tau = 2.1$ μs), which are comparable to those observed in the cyclometalated dipyridylbenzene Pt complexes.[29] The red shift of the peak wavelength and, hence the energy gap of **2b** and **c**, compared with that of **2a,** is a result of pyrazine substitution, for which the extra nitrogen atom of pyrazine lowers the π^* energy level of Pt(II) metal complexes. This ∼15 nm blue shift for **2c** versus that of **2b** is apparently caused by the methyl substituent, which destabilized the LUMO energy level by electron donation. Moreover, the lowest-energy absorption of **2d** appears at 463 nm with 5200 M^{-1} cm^{-1}, while the respective emission not only reveals a much larger Stokes shift but also possesses a distinctive vibronic-like progression with peak wavelengths at 584, 632, and 685 nm in THF solution (see Figure 3 and Table 3). The observed lifetime for **2d** in THF ($\tau = 13$ μs, $\Phi \sim 0.74$) is also substantially longer than those of **2a**−**c**, as well as those of complexes with a ^{3}MLCT in the lowest-lying manifold incorporating Os(II), Ir(III), or Pt(II) heavy ions and with a ^{1}MLCT state in proximity. Thus, for the case of **2d**, a significant amount of state mixing with the ligand-centered $^3\pi\pi$ transitions is expected.[30] This can be rationalized by the decrease of the π energy gap from the elongation of the π conjugation in **2d**. The progression of ≥1220 cm^{-1} for each successive peak of **2d** cannot be rationalized by the much smaller d-level splitting in a typical square planar Pt(II) complex, but it is similar to that corresponding to the C−C vibrational modes (1270−1300 cm^{-1}) for complexes involving terpyridyl ligands.[31]

On the other hand, the solution absorption and solid-state emission spectra of complexes **2a**, **3a** and **b**, **4**, and **5** are depicted in Figure 4. It is notable that all of the Pt(II) complexes shown in Figure 4 possess 2-pyridyl substituents; hence, the corresponding photophysical properties would reflect the influence of the anionic azolate segment (i.e., pyrazolate or triazolate) as well as the associated alkyl or fluoroalkyl substituents. For the UV−vis absorption spectral

(26) Gianini, M.; Forster, A.; Haag, P.; von Zelewsky, A.; Stoeckli-Evans, H. *Inorg. Chem.* **1996**, *35*, 4889.
(27) Whittle, C. E.; Weinstein, J. A.; George, M. W.; Schanze, K. S. *Inorg. Chem.* **2001**, *40*, 4053.
(28) Lin, Y. Y.; Chan, S. C.; Chan, M. C. W.; Hou, Y. J.; Zhu, N.; Che, C. M.; Liu, Y.; Wang, Y. *Chem.—Eur. J.* **2003**, *9*, 1263.
(29) Williams, J. A. G.; Beeby, A.; Davies, E. S.; Weinstein, J. A.; Wilson, C. *Inorg. Chem.* **2003**, *42*, 8609.
(30) (a) Sacksteder, L.; Zipp, A. P.; Brown, E. A.; Streich, J.; Demas, J. N.; DeGraff, B. A. *Inorg. Chem.* **1990**, *29*, 4335. (b) Sacksteder, L.; Lee, M.; Demas, J. N.; DeGraff, B. A. *J. Am. Chem. Soc.* **1993**, *115*, 8230.
(31) (a) Yang, Q. Z.; Wu, L. Z.; Wu, Z. X.; Zhang, L. P.; Tung, C. H. *Inorg. Chem.* **2002**, *41*, 5653. (b) Yam, V. W. W.; Tang, R. P. L.; Wong, K. M. C.; Cheung, K. K. *Organometallics* **2001**, *20*, 4476.

measurements, a significant blue shift of the MLCT absorption was noted by substituting trifluoromethyl or heptafluoromethyl for a *tert*-butyl group. This is shown by observation of two lowest-energy MLCT transitions at 377 and 389 nm as well as at 376 and 388 nm for the fluorinated complexes **3a** and **b**, respectively, for which both peaks show a substantial blue shift compared to those (416 and 442 nm) of *tert*-butyl complex **2a**. The decrease in the energy gap of the MLCT transitions is apparently caused by the electron-withdrawing effect of CF_3 and C_3F_7 substituents, which increases the π^* acidity of the pyrazolate anion, accompanied by lowering the Pt(II) metal 5d energy level. Concomitantly, the higher energy $\pi\pi^*$ transitions of **3a** and **b**, which are located at the UV region, also display a similar hypsochromic shift resulting from the increase of the intraligand $\pi\pi^*$ energy gap. For the triazolate complexes **4** and **5**, the respective MLCT transitions are also shifted to the higher-energy region versus those of the *tert*-butyl- and CF_3-substituted pyrazolate counterparts **2a** and **3a**, respectively. This delineation is consistent with a theoretical approach based on time-resolved density function theory calculation (not shown here), the results of which reveal that the HOMO is located at both the metal and azolate fragments, while the LUMO is located at the pyridyl fragment. Therefore, the substitution of, for example, the *tert*-butyl substituent with CF_3 (or C_3F_7) at the azolate fragment mainly lowers both the metal 5d and azolate π orbitals contributing to the HOMO resulting in an increase of the energy gap.

The photoluminescence spectra of **3a** and **b**, **4**, and **5** were measured in a degassed THF solution at room temperature; however, the emission is extremely weak ($\Phi \ll 10^{-3}$) and is supported by the phosphorescence lifetime of <10 ns in the degassed solution (not shown here). Although the associated deactivation mechanism, at this stage, is still pending for resolution, because of a strong tendency of the Pt−Pt interaction, self-quenching via the aggregation effect cannot be eliminated. Unfortunately, the poor solubility makes concentration-dependent studies unfeasible. In sharp contrast, moderate to highly intense luminescence was obtained with λ_{max} located at 595, 552, 564, and 544 nm for **3a** and **b**, **4**, and **5**, respectively, in the vacuum-deposited thin films (Figure 4). The structured emission of **2a** recorded in the solid state at room temperature, which shows three vibronic peaks at 489, 518, and 550 nm, is also depicted here as a reference. In comparison, the intensity ratio for these three vibronic peaks is appreciably different from that in fluid solution (see Figure 3 vs Figure 4). In addition, the highest-energy emission peak in **2a** undergoes an ~5 nm (207 cm^{-1}) blue shift in the solid state, while the other vibronic maxima remain nearly unchanged. One possible interpretation, in which the thin film emission of **2a** may consist of dual or multiple origins, has been discarded because of the similar spectral feature of **2a** in a 77 K solid film (not shown here). Alternatively, this discrepancy may more plausibly be rationalized by different sites of **2a** in the solid film so that the vibronic peaks, especially the 0−0 onset, are subject to environmental (inhomogeneous) perturbation.

Scheme 1

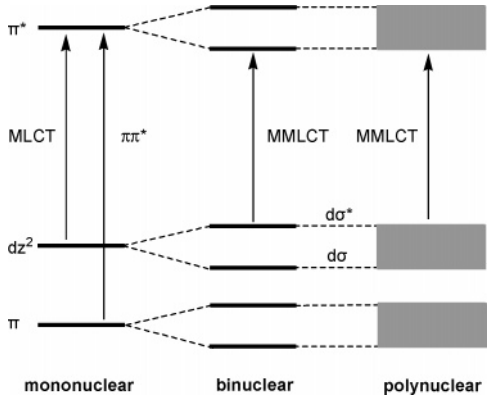

One remarkable feature is that the phosphorescence of complexes **3**−**5** exhibits a featureless line shape and a broader full width at half-maximum (fwhm), a phenomenon commonly encountered in the Pt(II) complexes, symbolizing the formation of either an excimer or an oligomer.[32] Moreover, except for **2a**, the emission showed a very large spectral shift with almost no spectral overlap between the lowest-energy MLCT absorptions (in fluid solution) and the onset of the phosphorescent emission signals (in solid film). This observation leads us to conclude that these phosphorescences primarily originate from the distinctive metal−metal-to-ligand charge-transfer transition (^{3}MMLCT or the [d_{σ^*},π^*] notation),[33] in line with that proposed by Miskowski and co-workers.[34] The short Pt···Pt contact observed in the columnar structure of **3b** sheds light on the expected destabilization of the metal 5d orbitals, resulting in a drastic peak-to-peak shift between the mononuclear absorption (in solution) and the polynuclear emission (in solid film) (Scheme 1).

These intriguing solid-state photophysical properties are consistent with those of the Pt(II) complexes [Pt(diimine)X_2], X = CN.[24] In the literature, it was reported that when two [Pt(diimine)X_2] units are in close enough proximity that they allow direct Pt−Pt interaction, a low-energy photoluminescence that is red-shifted from the ^{3}MLCT or $\pi\pi^*$ emission of mononuclear one becomes observable. The diagram illustrating the formation of columnar $\pi-\pi$ stacking and the Pt−Pt interaction in the solid state versus that of the respective MO energy levels is depicted in Scheme 1. We expected that, for complex **3a**, after the formation of linear Pt−Pt−Pt crosstalk, notable perturbation would be introduced and the electronic transition associated with this binuclear species would best be represented as the MMLCT transition (or the [d_{σ^*},π^*] notation). However, in view of the infinite columnar structure of **3b**, we speculate that the resulting MO energy levels would become more closely spaced in the crystal lattice, forming a quasi-continuum of levels (or bands) of very closely spaced orbitals, as shown in the right-hand side of this simplified MO energy diagram.[35]

(32) (a) Lai, S. W.; Chan, M. C. W.; Cheung, T. C.; Peng, S. M.; Che, C. M. *Inorg. Chem.* **1999**, *38*, 4046. (b) Lai, S. W.; Chan, M. C. W.; Cheung, K. K.; Che, C. M. *Inorg. Chem.* **1999**, *38*, 4262.

(33) (a) Lai, S. W.; Che, C. M. *Top. Curr. Chem.* **2004**, *241*, 27. (b) Lu, W.; Chan, M. C. W.; Zhu, N.; Che, C. M.; Li, C.; Hui, Z. *J. Am. Chem. Soc.* **2004**, *126*, 7639.

Table 4. Performance Characteristics for the Electrophosphorescence Devices Based on Complexes **2a** and **3a**

	concentration (%)	max lum (V)[a]	QE (%)[b]	PE (lm/W)[b]	LE (cd/A)[b]	λ_{max} (CIE)[c]
2a	6	27114 (15.0)	2.926	3.453	8.558	502 (0.21, 0.52)
	20	25957 (15.0)	2.174	2.861	6.942	514 (0.26, 0.54)
	50	24163 (12.4)	1.570	2.724	5.272	518 (0.28, 0.57)
	100[d]	16084 (12.0)	1.609	3.463	5.099	556 (0.41, 0.53)
3a	7	23023 (15.0)	4.202	4.555	14.031	552 (0.38, 0.54)
	20	40973 (15.0)	5.965	6.443	19.702	560 (0.42, 0.53)
	50	31086 (15.0)	1.478	1.818	4.690	574 (0.46, 0.51)
	100	19135 (15.0)	2.089	1.914	3.798	616 (0.56, 0.39)

[a] Values in the parentheses are the applied driving voltage. [b] Data collected at 20 mA/cm^2. [c] Measured at the driving voltage of 8 V. [d] A 14 nm thick pure layer was used.

Moreover, complex **3a**, which has the CF_3 substituents, exhibits a 43 nm (or 1310 cm^{-1}) bathochromic shift in emission peak λ_{max} versus that of complex **3b**, which has the C_3F_7 substituents. This result can be rationalized by an increase in the columnar $\pi-\pi$ stacking interaction because of the decrease of the steric hindrance for the CF_3 groups, as their electron-withdrawing character was somewhat comparable to or slightly less than that of C_3F_7. In contrast, for complex **5**, an even more notable hypsochromic shift of 51 nm (1575 cm^{-1}) was observed versus that of **3a**. This is apparently caused by the blue shift of the lowest-energy MLCT absorption while a similar degree of $\pi-\pi$ stacking was maintained. Empirically, we speculate that the degree of $\pi-\pi$ stacking for **5** can be qualitatively estimated using the difference in the Stokes energy shift of $\Delta E = 8570$ cm^{-1} versus that of **3a** ($\Delta E = 8900$ cm^{-1}). Note that this calculation was done by subtracting the emission peak (in cm^{-1}) of the solid sample from the lowest-energy absorption peak (in cm^{-1}) in fluid solution. Finally, it is also noteworthy that the emission peak, λ_{max}, of **4** occurs at 564 nm, and hence a ΔE value of 6080 cm^{-1} was deduced. The smaller ΔE may be attributed to a combination effect incorporating a larger steric interaction and a greater electron-donating character for the *tert*-butyl substituents.

OLED Fabrication. The superior thermal stability renders our Pt(II) complexes suitable for high performance OLED applications. Multilayer devices of the configuration ITO/NPB(40 nm)/CBP:**2a**(30 nm)/BCP(10 nm)/Alq_3(30 nm)/LiF-(1 nm)/Al(150 nm) were prepared with doping concentrations of **2a** of 6, 20, 50, and 100% neat film composition. This configuration was adopted from those reported by Thompson and Forrest.[36] Very bright emissions were observed for all doping concentrations, including the one with a pure layer of **2a**. Table 4 summarizes the selected performance data for these OLED devices. The $I-V-L$ curves, plotted in Figure 5, show a trend of increasing current density with increasing concentration of **2a**. A similar dependence on concentration was observed previously,[6,11] and this result implies that with the device mainly operated by charge trapping mechanism,[37] the more traps that are present, the higher current will be. Moreover, the EL spectra exhibit a large red shift of λ_{max} with increasing dopant concentration, 502, 514, 518, and 556 nm for devices with 6, 20, 50, and 100% dopant concentration (Figure 6). This may be attributed to the formation of excessive $\pi-\pi$ stacking interactions between the Pt(II) emitting molecules, for which a reduced red-shift of the EL emission maxima (600−626 nm) has been reported in the Ir(III)-based OLEDs upon increasing dopant concentrations from 7 to 100%.[38] Concurrently, the fwhm of the EL signal increased from 60 to 102 nm. It is notable that the 6% doped device showed the highest external QE at a lower current density but decreased rapidly upon

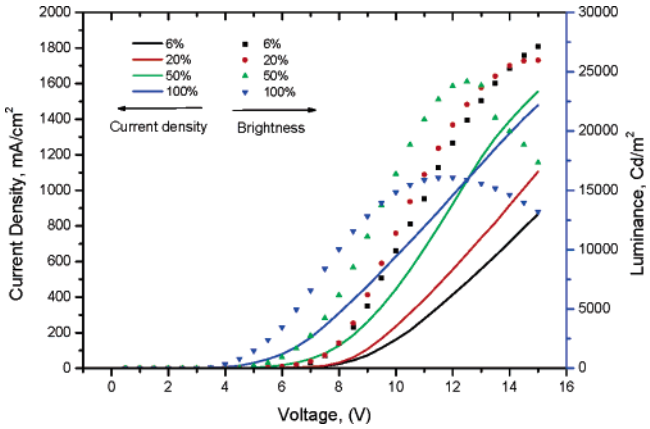

Figure 5. $I-V-L$ characteristics of OLED device ITO/NPB/CBP:**2a**/BCP/Alq/LiF/Al as a function of dopant concentration.

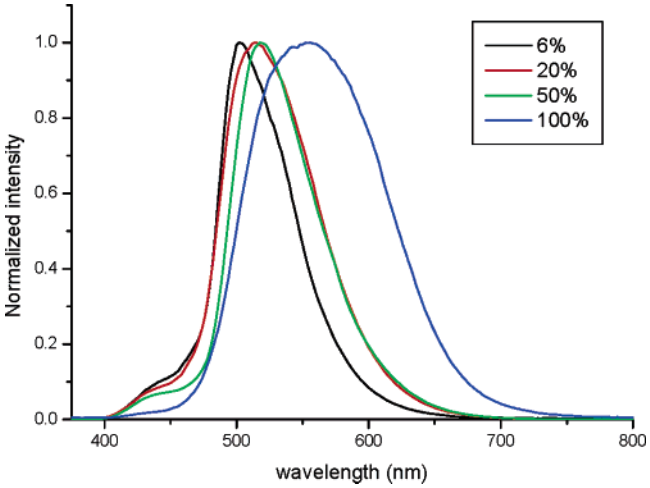

Figure 6. EL spectra of OLED device ITO/NPB/CBP:**2a**/BCP/Alq/LiF/Al as a function of dopant concentration.

(34) (a) Houlding, V. H.; Miskowski, V. M. *Coord. Chem. Rev.* **1991**, *111*, 145. (b) Miskowski, V. M.; Houlding, V. H. *Inorg. Chem.* **1991**, *30*, 4446.
(35) (a) Gliemann, G.; Yersin, H. *Struct. Bonding* **1985**, *62*, 87. (b) Yersin, H.; Riedl, U. *Inorg. Chem.* **1995**, *34*, 1642.
(36) Adachi, C.; Baldo, M. A.; Forrest, S. R.; Thompson, M. E. *Appl. Phys. Lett.* **2000**, *77*, 904.
(37) Gong, X.; Ostrowski, J. C.; Moses, D.; Bazan, G. C.; Heeger, A. J. *Adv. Funct. Mater.* **2003**, *13*, 439.
(38) Song, Y. H.; Yeh, S. J.; Chen, C. T.; Chi, Y.; Liu, C. S.; Yu, J. K.; Hu, Y. H.; Chou, P. T.; Peng, S. M.; Lee, G. H. *Adv. Funct. Mater.* **2004**, *14*, 1221.

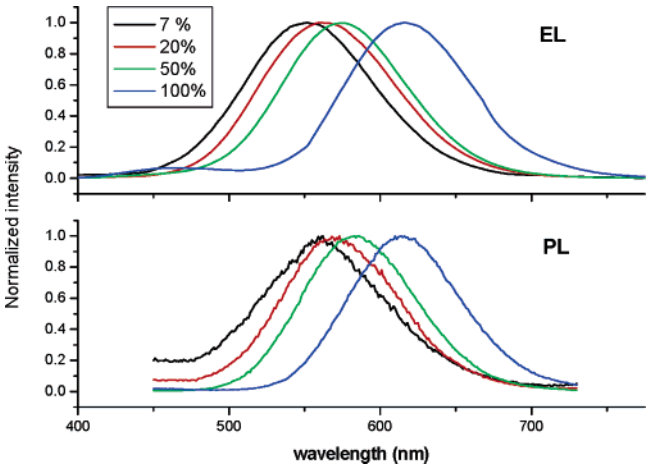

Figure 7. (a) EL spectra of OLED device ITO/NPB/CBP:**3a**/BCP/Alq/LiF/Al as a function of dopant concentration, and (b) PL spectra of **3a** embedded in the CBP matrix with variable dopant concentration.

increasing of the driving current. Moreover, the higher doping levels resulted in a much lower initial QE, along with a reduced dependence on the driving current. The existence of bulky *tert*-butyl substituents may have the capability to suppress the self-quenching activities,[39] thus maintaining the amorphous property during fabrication.[40]

Complex **3a** was also selected for use in fabricating similar multilayer OLED devices. As shown in Table 4, the doping levels were 7, 20, 50, and 100%, among which the best device performance with external QE $\approx$ 6% was observed for an intermediate doping level of 20%. Moreover, a significant red shift in the EL maxima from 552 to 616 nm was observed with increasing dopant concentration (Figure 7a). It is believed that the large concentration-dependent red-shift of emission maxima is caused by the self-aggregation of the Pt(II) dopant in the thin film during device fabrication; such a tendency has been revealed by the solid-state X-ray structural study in the previous section. In addition, for the device employing 100% Pt(II) dopant **3a**, a weak emission peak located at ~460 nm, probably originating from NPB, was clearly observed. This could be attributed to the enhanced electron conductivity of the CF_3 carrying **3a** in a manner such that electron injection into the NPB layer occurred when a neat film of **3a** was used.

For a further comparison, the observed red-shifted emission with increasing dopant concentrations in EL spectra was also observed in the PL spectra of the same series of doped CBP films (Figure 7b), substantiating the similar origin of the red-shifted emission (i.e., self-aggregation of the dopant). This observation is related to the basic behaviors of the square planar Pt(II) complexes, for which self-aggregation is invoked in oligomerization and excimer formation for several mononuclear Pt(II) complexes in solution. Thus, the detected luminescence would display features involving both ^{3}MLCT and ^{3}MMLCT excited states which are generated from the monomer and the oligomeric counterpart, respectively.[41] Analogously, the related bathochromatic shift observed for the green-emitting complex **2a**-based devices can be attributed to a similar effect.

Conclusion. We have demonstrated the synthesis of a series of square planar light-emitting complexes by treatment of pyridyl azolate ligands with Pt(II) reagents such as K_2PtCl_4 or $PtCl_2(DMSO)_2$. The procedures are efficient and suited to a variety of ligand modifications, demonstrating the versatility of our rational design and the effectiveness of derivatization in this class of compounds. Photoluminescence studies reveal that these complexes exhibit fairly high emission quantum yields in fluid solution or in the solid state, short phosphorescence radiative lifetimes in the range of several microseconds, and more importantly, a tuneable tendency to form aggregates, depending on the azolate ligands. The pyrazolate complexes **1** and **2** exhibited a slipped-stack arrangement with a negligible intermolecular Pt···Pt contact. This was confirmed by the X-ray structural analysis on **2c** and the relatively higher solubility in organic solvents. Their emissions, recorded in solution, may be attributed to ^{3}MLCT, $^3\pi\pi$, or mixing ^{3}MLCT/$^3\pi\pi$ character, in view of their overall spectral profile and the associated radiation lifetimes. In sharp contrast, a strong intermolecular $\pi-\pi$ stacking interaction is detected between the electron-rich azolate fragment and the electron deficient pyridyl group in complexes **3**−**5** giving an essentially linear columnar stacking arrangement in the solid state. The existence of notable intermolecular Pt−Pt contacts results in the formation of ^{3}MMLCT excited states that account for the observed photophysical properties in complexes **3**−**5** in the solid state.

Moreover, these Pt(II) complexes are suitable light-emitting materials, especially as phosphorescent dopants for OLED applications, because of their intense, readily tuneable emission hues and good thermal stability. For ^{3}MLCT/$^3\pi\pi$ emitters such as **2a**, the best device performance was realized using a 6% doping concentration. An external quantum efficiency of 2.9%, a luminous efficiency of 8.6 cd/A at 20 mA/cm^2, and a luminescence of 27114 cd/m^2 at an applied voltage of 15 V were realized. With the ^{3}MMLCT emitters such as **3a**, the best device performances are achieved at an ~20% dopant concentration, along with an external quantum efficiency of 6.0%, and a luminous efficiency of 19.7 cd/A at 20 mA/cm^2. These results are remarkable in that they show promise for OLED applications based on these Pt(II) emitting materials.

Acknowledgment. This work was funded by the National Science Council of Taiwan, R.O.C., under Grants NSC 93-2113-M-007-012 and NSC 93-2752-M-002-002-PAE.

Supporting Information Available: X-ray crystallographic data file (CIF) of complexes **2c** and **3b**. This material is available free of charge via the Internet at http://pubs.acs.org.

IC051393B

(39) Xie, H. Z.; Liu, M. W.; Wang, O. Y.; Zhang, X. H.; Lee, C. S.; Hung, L. S.; Lee, S. T.; Teng, P. F.; Kwong, H. L.; Zheng, H.; Che, C. M. *Adv. Mater.* **2001**, *13*, 1245.
(40) Ostrowski, J. C.; Robinson, M. R.; Heeger, A. J.; Bazan, G. C. *Chem. Commun.* **2002**, 784.
(41) Lai, S. W.; Chan, M. C. W.; Cheung, T. C.; Peng, S. M.; Che, C. M. *Inorg. Chem.* **1999**, *38*, 4046.